Atmos. Meas. Tech. Discuss., doi:10.5194/amt-2016-246, 2016
Manuscript under review for journal Atmos. Meas. Tech.
Published: 25 October 2016

Atmospheric Measurement Techniques
Discussions
Open Access

Analysis of geostationary satellite derived cloud parameters associated with high ice water content environments .

Adrianus de Laat[1], Eric Defer[2], Julien Delanoë[3], Fabien Dezitter[4], Amanda Gounou[5], Alice Grandin[4], Anthony Guignard[3], Jan Fokke Meirink[1], Jean-Marc Moisselin[5], and Frédéric Parol[6]

[1]KNMI, de Bilt, The Netherlands
[2]Laboratoire d'Aérology, CNRS/OMP Toulouse, France
[3]Laboratoire Atmosphère, Milieux et Observations Spatiales, UVSQ, Guyancourt, France
[4]AIRBUS, Toulouse, France
[5]Meteo France, Toulouse, France
[6]Laboratoire d'Optique Atmosphérique, Université de Lille, Sciences et Technologies, Villeneuve d'Ascq, France

correspondence to: Adrianus de Laat (laatdej@knmi.nl)

Atmos. Meas. Tech. Discuss., doi:10.5194/amt-2016-246, 2016
Manuscript under review for journal Atmos. Meas. Tech.
Published: 25 October 2016

Abstract

We present a newly developed high ice water content mask (High IWC) based on measurements of the cloud physical properties (CPP) algorithm applied to the geostationary Meteosat Second Generation (MSG) Spinning Enhanced Visible and Infrared Imager (SEVIRI). The mask was developed within the European High Altitude Ice Crystals (HAIC) project for detection of upper atmospheric high IWC, which can be a hazard for aviation.

Evaluation of the High IWC mask with satellite measurements of active remote sensors of cloud properties (CLOUDSAT/CALIPSO combined in the DARDAR product) shows that the High IWC mask can be fine-tuned for detection of high IWC values > 1 g/m^3 in the DARDAR profiles. The best CPP predictors of High IWC were the condensed water path, cloud optical thickness, cloud phase, and cloud top height. The evaluation of the High IWC mask against DARDAR provided some indications that the MSG-CPP High IWC mask is more sensitive to cloud ice or cloud water in the upper part of the cloud, which is relevant for aviation purposes. Biases in the CPP results were also identified, in particular a solar zenith angle (SZA) dependence that reduces the performance of the High IWC mask for SZAs > 60°. Verification statistics show that for the detection of High IWC a trade-off has to be made between better detection of High IWC scenes and more false detections, *i.e.* scenes identified by the High IWC mask that do not contain IWC > 1 g/m^3. However, the large majority of these detections still contain IWC values between 0.1-1 g/m^3.

Comparison of the High IEC mask against results from the Rapid Developing Thunderstorm (RDT) algorithm applied to the same geostationary SEVIRI data showed that there are similarities and differences with the High IWC mask: the RDT algorithm is very capable of

Atmos. Meas. Tech. Discuss., doi:10.5194/amt-2016-246, 2016
Manuscript under review for journal Atmos. Meas. Tech.
Published: 25 October 2016

Atmospheric Measurement Techniques Discussions

detection young/new convective cells and areas, whereas the High IWC mask appears to be better capable of detecting more mature and ageing convection as well as cirrus remnants. The lack of detailed understanding what causes aviation hazards related to High IWC hampers further tuning of the High IWC mask. Additional evaluation of the High IWC mask against field campaign data should provide more information on the performance of the MSG-CPP High IWC mask and contribute to a better characterization.

Atmos. Meas. Tech. Discuss., doi:10.5194/amt-2016-246, 2016
Manuscript under review for journal Atmos. Meas. Tech.
Published: 25 October 2016

1. Introduction

Weather hazards can have a significant impact on aviation via disturbing flight schedules and causing air traffic delays, but also as a cause of accidents, some of them fatal. Among the weather related effects on aviation are changes in visibility like fog, clouds, rain, snow, hail, wind, turbulence, lightning, smoke and volcanic ash [Perkins et al., 1998; Bragg et al., 2002; Mecikalski et al., 2007]. One particular hazardous process is in-flight or in-service icing. Aircraft may penetrate clouds of super-cooled water droplets, or high densities of ice particles. The droplets or particles may deposit on cold aircraft surfaces, affecting aerodynamic properties of the plane, the engine performance, or inlets and nozzles used for onboard monitoring of environmental conditions, the latter resulting in a malfunctioning of for example speed sensors [Mason et al., 2006; Mecikalski et al., 2007].

The microphysical conditions under which in-service icing may occur are generally well understood: either large amounts of super-cooled cloud droplets are present, or high concentrations of ice particles. However, what the corresponding general atmospheric conditions are, and how to identify or diagnose them, has been a much more difficult task. This is in part related to the notion that the majority of in-service icing events appear to occur outside of what is called "classic" convection, *i.e.* areas of vigorous updrafts [Grzych and Mason, 2010]. Approximately only 20% of in-service icing events are associated with this "classic" convection. The remaining 80% appears to be related to occurrence of ice crystals in anvils, with only weak or moderate convection and turbulence. Such systems are characterized by large concentrations of small particles rather than large particles (hail) and/or super-cooled water droplets.

Atmos. Meas. Tech. Discuss., doi:10.5194/amt-2016-246, 2016
Manuscript under review for journal Atmos. Meas. Tech.
Published: 25 October 2016

Furthermore, areas of large concentrations of small ice particles are difficult to detect by on-board radar, in contrast to the "classical" convection where the deep convection and vigorous cores can be detected by on-board radar and thus can be avoided. Finally, it appears that the majority of in-service icing events are occurring in tropical and subtropical regions of the world (30N-30S), although potential in-service conditions can occur at higher latitudes [Grzych and Mason, 2010].

To address many of the issues related to in-service icing events and in anticipation of regulation changes regarding mixed phase and glaciated icing conditions, the large European High Altitude Ice Crystals project (HAIC) was initiated in 2012 to investigate a wide range of aspects of in-service icing. The HAIC project combines laboratory experiments (wind chambers), field campaigns, numerical modeling and remote sensing techniques to study a variety of aspects of in-service icing.

Laboratory measurements focus on the characterization, optimization, enhancement and selection of the most sophisticated cloud microphysics probes in order to measure mixed phase and glaciated icing conditions during flight tests and to calibrate icing wind tunnels. Furthermore, the HAIC project aims at measurement and characterization of the microphysical properties of core or near-core regions of deep convective clouds, including cloud liquid and ice water contents and particle size and shape distributions. Finally, HAIC aims at characterizing the atmospheric conditions for possible in-service icing and the detection of such areas in satellite remote sensing products.

An important aspect of the HAIC project is the development of space-borne remote detection and now-casting application of glaciated icing conditions based on imagery of geostationary MSG - SEVIRI (Meteosat Second Generation - Spinning Enhanced Visible and InfraRed Imager) satellite observations. Atmospheric conditions under which in-service icing occurs are not well understood nor well characterized – which is also the prime justification for the HAIC project. However, it is widely accepted that the presence of High Ice Water Content is a crucial condition for the occurrence of in-service icing. Detection of areas of potential High Ice Water Content by satellite remote sensing thus provides important spatio-temporal information for the possible occurrence of in-service icing events.

In this paper, we present a new High Ice Water Content mask (High IWC mask) based on the output of the MSG - Cloud Physical Properties (CPP) algorithm [Roebeling et al., 2006; Meirink, 2013] that was developed within the Climate Monitoring Satellite Application Facility (CMSAF) of the EUropean METeorological SATellite organization (EUMETSAT), and applied to the geostationary SEVIRI satellite measurements. The CPP algorithm provides a number of cloud physical properties that are of interest in diagnosing possible in-service icing conditions. The high IWC mask will be derived and evaluated against measurements of cloud properties from active remote sensing instruments on board of satellites, and finally the high IWC mask will be compared with the EUMETSAT SEVIRI Rapid Development Thunderstorm (RDT) product that is used to identify rapidly growing thunderstorms and convective systems [Autonès, 2012].

2. Project description and datasets used.

2.1 HAIC

Within the European FP7 HAIC project, academics and aeronautic industries are collaborating within six main research activities that include dedicated field campaigns, development of new in situ probes, space-based detection and monitoring, upgrade of on-board weather radars, improvement of ground test facilities, and modeling of melting and impingement processes. All activities are designed to enhance aircraft safety when flying in mixed phase and glaciated icing conditions.

The HAIC Sub-Project 3 (SP3), entitled Space-borne Observation and Nowcasting of High Ice Water Content Regions, focuses on the development of space-borne remote detection of high Ice Water Content (IWC) and nowcasting techniques to support the second and third HAIC flight campaigns and ultimately provide relevant near real-time weather information through Air Traffic Management (ATM). The SP3 investigations are divided in three interacting Work Packages (WPs): (i) Geostationary space-borne retrievals of high IWC events focusing on the detection of high IWC cloud regions mainly from the SEVIRI imager on MSG in daytime; (ii) Polar orbiting space-borne retrievals of high IWC events investigating the detection of high IWC cloud regions from visible, infrared and microwave passive and active observations of the space-based A-Train mission; (iii) Nowcasting of tropical convection dedicated to the tracking of deep convection over the Tropical Atlantic for operational applications based on the Rapid Development Thunderstorm (RDT) nowcasting tool. Following the HAIC Technology Readiness Level (TRL) strategy, the SP3 activities are required to pass with success three TRL levels: TRL3 (characteristic proof of concept), TRL5 (breadboard validation in relevant environment) and TRL6 (prototype demonstration in a relevant environment).

2.2 MSG-CPP

The CPP algorithm [Roebeling et al., 2006; Meirink, 2013] uses SEVIRI's visible (VIS) and near-infrared (NIR) measurements to retrieve cloud optical thickness (τ) and cloud particle

Atmos. Meas. Tech. Discuss., doi:10.5194/amt-2016-246, 2016
Manuscript under review for journal Atmos. Meas. Tech.
Published: 25 October 2016

Atmospheric Measurement Techniques Discussions

effective radius (r_e) by applying the classical Nakajima and King [1990] approach. This approach is based on the basic feature that the reflectance at a for cloud particles non-absorbing wavelength is primarily related to τ, while the reflectance at an absorbing wavelength is mainly related to r_e. For SEVIRI retrievals the VIS 0.64 µm and the NIR 1.63 µm channels have been used here as non-absorbing and absorbing channels, respectively. Around 1.63 µm ice particles are more absorbing than water droplets, which is not the case at 0.64 µm. Hence, together with the use of a thermal infrared (IR) window channel to inform on cloud top temperature, this allows to retrieve cloud thermodynamic phase.

CPP is based on look-up tables (LUTs) of top-of-atmosphere (TOA) reflectances for single-layer, plane parallel, water and ice clouds, simulated by the Doubling Adding KNMI (DAK) radiative transfer model [Stammes, 2001]. Single scattering properties have been calculated using Mie theory for spherical water droplets and ray tracing for imperfect hexagonal ice crystals [Hess et al., 1998], respectively. Absorption by atmospheric trace gases is taken into account based on Moderate Resolution Atmospheric Transmission code simulations (MODTRAN4 Version 2 [Anderson et al., 2001]). For cloudy pixels (cloud contaminated or cloud filled, as determined by the cloud mask described in Roebeling et al. [2006]) τ and r_e are retrieved by matching the observed reflectance to the LUTs. First the ice cloud LUT is tried. If this leads to a match and if the cloud top temperature – retrieved from the 10.8 µm channel - is below 265 K, the thermodynamic phase is set to ice. Otherwise, the water cloud LUT is used, and the phase is set to liquid. Liquid and ice water path (LWP and IWP) are then calculated following Stephens [1978]:

$$LWP = \frac{4}{3Q_e}\rho_l \, r_e \tau; \qquad \mathrm{IWP} = \frac{4}{3Q_e}\rho_i \, r_e \tau \qquad (1)$$

where Q_e is the extinction efficiency at visible wavelengths (set to 2), and ρ_l and ρ_i are the densities of water and ice, respectively. Eq. (1) assumes a vertically homogeneous distribution of cloud condensate. CPP uses surface albedo at the VIS and NIR channels based on MODIS [Moody et al., 2005], and water vapour path from the ERA-Interim reanalysis project [Dee et al., 2011] of the European Center for Medium range Weather Forecast (ECMWF) as ancillary input data. Cloud property retrievals become very uncertain at high solar zenith angles (θ_0) and viewing zenith angles (θ). Therefore, no retrievals are performed for $\theta_0 > 78°$ or $\theta > 78°$. Earlier versions of CPP have been extensively validated using ground-based observations [Roebeling et al., 2008; Wolters et al., 2008) and used for the evaluation of regional climate models [Roebeling and van Meijgaard, 2009; Greuell et al., 2011]. Note that the CPP parameters associated with reflected solar radiation are mostly representative for the upper parts of clouds, in particular in case of optically thick clouds (*e.g.* deep convection). Because of the reliance of CPP on reflected solar radiation most of the photons are reflected back from the upper parts of optically thick clouds [Platnick, 2000]. Hence, little information from deep within optically thick clouds can be obtained. Also note that unpublished results indicate that CPP R_{eff} does not correlate very well with remote sensing profiles of R_{eff}. Furthermore, the physical interpretation of R_{eff} is rather complicated and care should be taken with interpreting R_{eff} as representative for real-world cloud particles sizes, in particular for ice clouds [*e.g.* McFarquhar and Heymsfield, 1998; Mitchell et al. 2011]. Detailed information on the CPP version used can be found in Meirink [2013].

2.3 DARDAR

DARDAR (raDAR/liDAR) [Delanoë and Hogan, 2008, 2010] consists in two synergistic products derived from the combination of the CloudSat radar [Stephens et al., 2002] and CALIPSO lidar [Winker et al., 2009] measurements. These products are distributed through the ICARE centre in Lille (France). The first one, DARDAR-MASK [Delanoë and Hogan, 2010, Ceccaldi et al 2013], is mainly a target classification of the scene observed by both CloudSat and CALIPSO. More precisely the DARDAR-MASK data set employs a combination of the CloudSat, CALIPSO measurements to identify cloud, precipitation and aerosol presences and also retrieve cloud phase properties. The algorithm, based on a decision tree, was originally designed to identify ice clouds on the basis of the synergy of surface-based radar, lidar observations. The DARDAR-MASK returns a range of categories: clear, ground, stratospheric features, insects, aerosols, rain, super-cooled liquid water, liquid warm, mixed-phase and ice. The algorithm also permits an "unknown" classification when it is not possible to determine one of these categories [Delanoë and Hogan, 2010]. This commonly occurs in regions where the radar and lidar signal have been heavily attenuated or are missing. DARDAR-MASK used CALIPSO backscatter and temperature to identify super-cooled water in the 0°C to −40°C range [Ceccaldi et al 2013], while the depolarization is considered too noisy to be used at the CALIPSO resolution [Delanoë and Hogan, 2010].

Ice cloud properties are available in the second DARDAR-CLOUD product [Delanoë and Hogan, 2010]. This product uses the "varcloud variational technique" [Delanoë and Hogan, 2008] which combines the CloudSat radar and CALIPSO lidar profiles for retrieving the extinction coefficient, IWC and Re of the ice cloud. DARDAR-CLOUD assumes a "unified" PSD given by Delanoë et al. [2005, 2014]. The mass-size and area-size relations of non-spherical particles are considered using in situ measurements [Brown and Francis, 1995; Francis et al., 1998; Delanoë et al., 2014].

2.4 Rapid Development Thunderstorm (RDT; v2013)

RDT tracks clouds, identifies those that are convective, and provides a description of their microphysical, morphological and dynamical properties. In particular, it allows locating the boundaries of the cells and the overshooting tops when present. This last characteristic is of a great importance for aircraft safety as overshooting is associated with strong updrafts. The RDT also estimates the cell vertical extent, its horizontal growth rate and cooling rate necessary for estimating the intensification/decaying of the convective cell. The speed and direction of propagation are also provided. Two other important parameters are available in RDT product for icing issues: the main cloud phase of the convective cell and the highest convective rain rate inside the cell, both coming from other NWCSAF (Satellite Application Facility in Support to Nowcasting and Very Short Range Forecasting) algorithms and integrated into the RDT output. The RDT algorithm is based on four main modules: the detection, the tracking, the discrimination and the advection scheme. The RDT software is developed by Météo-France in the framework of NWCSAF.

RDT combines a cloud-tracker and an algorithm to discriminate convective and non-convective cloud objects. The cloud objects defined by the RDT are cloud towers with a significant vertical extension, namely at least 6°C colder than the warmest pixel in the surrounding [Guillou et al., 2009]. For that purpose, the 10.8 µm channel of MSG is used. The tracking algorithm allows linking an object on the previous image. Once the link is identified, some characteristics of the object can be calculated: trends (e.g. cooling rate), motion vector (considering successive positions of the gravity center). Then the third step is a statistical scheme to define if the cell is convective or not. The statistical scheme, called discrimination, depends on the available satellite data as well as historic data. In optimal configuration it requires for the following satellite channels: water vapor channels at 6.2 µm and 7.3 µm, thermal infrared channels at 8.7 µm, 10.8 µm, and 12.0 µm. Empirical rules help to classify convective systems. The coordinates of each cell are available as a polygon including associated characteristics. For the comparison with the MSG-CPP High IWC mask we focus on the agreement between the location of RDT objects and the High IWC mask.

2.5 AIRBUS In-Service event database

Within the HAIC project, AIRBUS has provided a global database of "In Service" events of icing, *i.e.* reports by pilots of flying conditions where icing apparently has affected flying conditions. Due to AIRBUS regulations the database is not public, but information can be obtained via AIRBUS in case of use for scientific research.

3. High IWC mask

3.1 Analysis of AIRBUS event database and development of a provisional High IWC mask.

Within the HAIC project, the AIRBUS "In Service" event database was used to construct a first provisional High IWC mask (v1). Details of its construction can be found in the Supplementary

Atmos. Meas. Tech. Discuss., doi:10.5194/amt-2016-246, 2016
Manuscript under review for journal Atmos. Meas. Tech.
Published: 25 October 2016

Information (SI). The mask is based on defining thresholds for a set of CPP parameters: only if all criteria are met, *i.e.* the CPP parameter values fall within the pre-defined threshold intervals, the SEVIRI pixel is masked as a High IWC event. The MSG-CPP parameter threshold values used for defining the High IWC mask v1 are listed in table 1. The number of useful events in the database is limited, casting doubts about the usefulness of the database and thereby the provisional High IWC mask v1. Hence, an alternative approach was agreed upon, whereby identification of high IWC values (> 1 g/m^3) in satellite vertical profile measurement if water content serves as a proxy for in service icing conditions.

3.2 Evaluation of MSG-CPP with DARDAR

For comparison between MSG-CPP and cloud profile measurements from radars and lidars on polar satellites we use DARDAR data, which combines vertical information from the CLOUDSAT radar and CALIPSO lidar measurements into one product. A test dataset for the year 2008 was made available containing orbits with sufficient high IWC measurements within one orbit, while orbits were required to fall within the SEVIRI disc during daytime (see supplementary information table S1). A total of 31 orbits were analyzed that cover all months and the entire SEVIRI disc.

Figure 1 shows an example of a DARDAR orbit and the corresponding MSG-CPP cloud top heights. Indicated are also the locations where the DARDAR profiles indicate ice clouds. Based on visual inspection there is a clear correspondence between the DARDAR ice identification and the MSG-CPP clouds. Note that because of the time it takes for one DARDAR orbit to circle the earth, and with a MSG-SEVIRI acquisition every 15 minutes, typically three to five MSG-CPP images cover the DARDAR orbit, and thus that for some DARDAR profiles the MSG-CPP image shown in Figure 1 is not the MSG-CPP output data nearest in time to the DARDAR measurement.

Figure 2 shows the same DARDAR orbit but now with the vertical ice water content profile and the corresponding MSG-CPP cloud top height (CTH). Also here there is a clear correspondence between mid-latitude DARDAR maximum ice cloud heights and MSG-CPP cloud top heights. However, within the tropics conditions MSG-CPP underestimates of DARDAR maximum ice cloud height frequently occur. This typically occurs for less dense cirrus and is related to the nature of the MSG-CPP cloud top temperature/height algorithm. It is a simple one-channel (10.8 micron) approach, which assumes opaque clouds. Top-of-atmosphere IR radiation for semi-transparent cirrus contains a significant contribution from the warm surface, leading to an overestimation of the cloud top temperature and underestimation of the height. Although less severe, such an underestimation of cloud top height and overestimation of cloud top temperature is typical for most SEVIRI-based algorithms, as evaluated in Hamann et al. [2014].

Figure 3 shows the probability distribution of DARDAR cloud top height (maximum level with IWC > 0) and MSG-CPP cloud top height as function of the MSG-CPP High IWC mask parameter threshold values. The parameters with the largest impact on the probability distribution are the CWP and the cloud top height and/or cloud top temperature, as was already shown before. Obviously the detection is sensitive to choice of height/temperature threshold in this comparison. To provide some background: low clouds and high (optically) thick cirrus clouds typically have a condensed water path of at maximum few hundred g/m^2. Optically thin cirrus clouds have typically a CWP of less than 100 g/m^2. Only for very deep and thick convective clouds the CWP exceeds 1000 g/m^2. When looking at specific CWP values, we see that a given threshold improves the comparison but that it is unclear which of the thresholds is better as the correlation between DARDAR and MSG-CPP cloud top heights hardly differ for different CWP thresholds (not shown).

To further investigate the CWP in both MSG-CPP and DARDAR, the DARDAR IWC profiles were converted to total IWP and then compared to the MSG-CPP CWP. Figure 4 shows the probability distribution of MSG-CPP and DARDAR IWP for the same data used for Figure 3. The probability distribution is clearly skewed, with DARDAR IWP being considerably larger than the MSG-CPP CWP. One possible explanation is that for its retrieval, the MSG-CPP algorithm assumes a vertically homogeneous distribution of effective radius and cloud condensate, which may be unrealistic. Because there is less reflected sunlight (information) coming from deeper in the clouds towards the satellite [Platnick, 2000], the satellite measurements will be more representative of the upper part of in particular deep convective clouds. However, the size of ice particles within geometrically thick clouds will generally be larger towards the cloud bottom [Feofilov et al., 2015] due to various processes (*e.g.* sedimentation and the higher water vapor pressure at lower altitudes). Hence, the MSG-CPP algorithm likely underestimates the average effective radius of these optically thick clouds. The parameterization of the MSG-CPP CWP depends linearly on the retrieved effective radius, possibly explaining the MSG-CPP underestimation of CWP.

To test this idea we further analyzed Figure 4 for its relation with the variability in the effective radius of the DARDAR profile. The root-mean-square (rms) value of the effective radius of the profile for where there is ice provides an indication of how uniform the effective radius distribution is throughout the profile. In Figure 5 the probability distribution of Figure 4 is filtered on the rms value of the DARDAR profile effective radius: the smaller the rms value, the more uniform the vertical distribution of the effective radius is and the more it can be expected that the DARDAR CWP/IWP agrees with MSG-CPP. Figure 5 shows that this indeed is the case. Furthermore, it appears that the vertical effective radius variability acts approximately as an offset: the fit lines through the data are more or less parallel to the 1:1 line.

The analysis performed in this section provides a proper characterization of the MSG-CPP data vs. DARDAR measurements, highlighting agreement as well as caveats. With this information, the next step is to investigate to what extent the first High IWC mask is capable of identifying high IWC values in the DARDAR IWC profiles, and whether the mask can be improved.

For Figure 6, DARDAR profiles were ranked according to the maximum IWC value in the profile, after which the percentage of DARDAR profiles identified by the High IWC mask was calculated. Clearly, the number of high IWC events identified by the High IWC mask is very limited. The insert shows the same data but for the different thresholds that are used for the High IWC mask. The most important limiting factor here is the CWP, with the CTH and/or CTT being of secondary importance. The latter is not surprising, as the maximum IWC value not necessarily is located higher up in the troposphere (either > 8 km or below 225 K). However, the limiting effect of choosing a high CWP as threshold means that a sensitivity analysis should be performed to see whether a more optimal set of MSG-CPP parameter thresholds can be defined for identification of high IWC events. Hence, similar analyses were performed for the following range of MSG-CPP parameter threshold values:

- Cloud water path is > 100-1000 g/m^2 with 100 g/m^2 steps
- Cloud top temperature < 275-225 K with 5 K steps.
- Cloud optical thickness 5-20 with steps of 5 units

Atmos. Meas. Tech. Discuss., doi:10.5194/amt-2016-246, 2016
Manuscript under review for journal Atmos. Meas. Tech.
Published: 25 October 2016

Atmospheric Measurement Techniques Discussions

The effective radius was left out as it is generally not representative for the effective radius at the level of the highest IWC occurrence (see earlier discussion). The cloud top height was left out as it is related to the cloud top temperature.

The subsequent statistic of identification of high IWC events by the High IWC mask as function of maximum IWC value in the DARDAR profile as shown in Figure 6 were then analyzed according to the following characteristics: the steepness of the increase in fraction of identified DARDAR profiles by the High IWC mask in the maximum IWC interval in the interval between 0.1 g/m^3 and 1 g/m^3, and the fraction of maximum DARDAR IWC > 1 g/m^3 identified by the High IWC mask.

3.3 Optimization of the MSG-CPP High IWC mask.

The best High IWC mask consists of those combinations of MSG-CPP parameters that identify DARDAR IWC > 1 g/m^3 while rejecting DARDAR IWC < 1 g/m^3. This is in essence a binary decision model – also known as a contingency model - as outlined in Table 2, which shows a prototypical contingency table for decision-making. Given that the large majority of MSG-CPP pixels will not be identified as high IWC events (see Figures 3, 5 and 6), we focus on the following three verification statistics: the Hit Rate or Probability Of Detection (POD), the False Alarm Ratio (FAR) and the Threat Score or Critical Success Index (CSI), the latter of which is often being used for low frequency events. These statistics can be used to objectively select the best combination of MSG-CPP parameters thresholds. Based on table 2, these three statistics are calculated as follows (see equation 1):

$$POD = \frac{A}{A+C} \qquad FAR = \frac{B}{A+B} \qquad CSI = \frac{A}{A+B+C} \qquad (2)$$

Figure 7 shows the probability distribution of the POD (upper panel), FAR (middle panel) and CSI (lower panel) for different MSG-CPP parameter threshold settings (see legend of Fig. 7 for more details). The probability distribution of PODs varies between 0 and 0.9, with a gradual decrease in occurrence of increasing POD. The probability distribution of the FAR starts only at 0.3, shows a distinct peak around 0.4 with a long tail up to values of 0.95, showing that to some extent 'false alarms' in MSG-CPP cannot be avoided. The CSI shows a broad distribution between 0 and 0.4.

If we look at the relation between the POD and FAR as well as between the POD and CSI – shown in Figure 8 - we see that increasing POD also results in increasing FAR, thus better detection of high IWC values in DARDAR IWC profiles by MSG-CPP is accompanied by an increasing number of 'false alarms'. The relation between the POD and the CSI shows this effect with a maximum around a POD value of 0.6 and a decreasing but also widening distribution of the CSI with increasing POD beyond 0.6, reflective of the problem of more false positives with a better probability of detection.

We now proceed to select threshold combination with a CSI close to the maximum CSI encountered in Figure 8 (CSI > 0.35). Table 3 shows the fraction of High IWC masks (or pixels) obtained for different MSG-CPP parameter thresholds for which the CSI was larger than 0.35. The CWP threshold is chosen at 100 g/m^2 as a higher value would exclude too many potential high IWC events. The CTT threshold is chosen to be < 270 K but not lower for the same reason, and 270 K is close to freezing point of water. The COT threshold is chosen at 20 or larger as we want to avoid too many optically thin clouds. Finally, there does not appear to be much of a relation between the height of the DARDAR high IWC maximum value and the ability of MSG-CPP to detect High IWC events.

Summarizing, we define the following MSG-CPP parameter thresholds for version 2 of the High IWC mask.

- The cloud phase ice
- The effective radius ***no threshold***
- Condensed water path > 100 g/m^2
- Cloud top height ***no threshold***
- Cloud top temperature < 270 K.
- Cloud optical thickness > 20

This combination of thresholds has a POD = 0.59, a FAR of 0.52 and a CSI of 0.36. For the same DARDAR data but with the High IWC mask v1 the numbers were: POD = 0.08, a FAR of 0.34 and a CSI of 0.08. Both the POD and CSI are better for v2 compared to High IWC mask v1. The FAR is better for v1 compared to High IWC mask v2, indicative of the trade-off between detection and false alarms as discussed in relation to Figure 8. The better POD and CSI are also reflected in the notion that the number of detections of DARDAR IWC profiles with maximum IWC > 1 g/m^3 is in High IWC mask v2 an order of magnitude larger than in High IWC mask v1 (see Figure 9).

We realize that there is no unique or best set of threshold values, as there are two competing interests: better detection of high IWC events *vs.* fewer false alarms. Furthermore, it is *a priori* not clear what the defining characteristics of an High IWC mask should be, as the number of real in-service icing events is rather limited. As it is unclear what the exact atmospheric conditions are for the occurrence of in-service icing are to begin with, there are no compelling arguments why to specifically choose for other threshold values as long as the favored statistic (CSI) is close to the maximum CSI found in the sensitivity analysis.

We also ran a test accounting for the time difference between the DARDAR measurement and the MSG-CPP measurement (once every 15 minutes). For the verification discussed here the DARDAR measurements were coupled to the nearest MSG-CPP measurement in space and time (which thus can be either before or after the DARDAR measurement). A test with either the nearest MSG-CPP measurement before the DARDAR measurement or the nearest MSG-CPP measurement after the DARDAR measurement did result in very similar verification statistics (change in all verification statistics less than 0.05).

We finally checked the verification statistics for the sub-MSG-CPP pixel average DARDAR profile and the parallax correction. The MSG-CPP pixel size – typically 5 km – is much larger than the footprint of DARDAR profile - typically 250 m. As a check, we ran the same verification for the MSG-CPP pixel average DARDAR profile. Obviously this results in fewer collocations. However, for only 10% - 2% - 0.1% of the DARDAR profiles with maximum IWC above 1 g/m^3, the maximum IWC in the corresponding average IWC profile was less than 1 g/m^3 - 0.5 g/m^3 – 0.1 g/m^3, respectively. As a result, the verification statistics were very similar with changes of 0.05 at maximum but generally less. Similar small changes in verification statistics were found when applying the parallax correction.

Figure 9 shows the results of the evaluation for the MSG-CPP High IWC mask with DARDAR IWC profile measurements. The higher the maximum IWC value, the larger the chances of detection by the High IWC mask. The results also show that the High IWC mask identifies the majority (50-60%) of the DARDAR profiles that we aim to detect (IWC > 1 g/m^3), compared to an identification rate of less than 10% with High IWC mask v1. In addition, the higher the altitude of maximum IWC in DARDAR, the higher the percentage of these cases identified by the High IWC mask v2, increasing to almost 80% for DARDAR maximum IWC altitudes > 8 km compared to 50-60% for all cases combined. This is consistent with earlier findings indicating that SEVIRI/MSG-CPP is more sensitive to the physical conditions of the upper part of a cloud. On the other hand, for the DARDAR cases with maximum IWC < 1 g/m^3 yet still identified by the High IWC mask v2 (false detections), the maximum IWC is for the majority of cases still > 0.1 g/m^3. In other words, for most false detections by the High IWC mask v2 the maximum IWC is still quite high, just not above the threshold value. Most of the false detections are thus not false in the sense that there is no IWC. If IWC values larger than 0.1 g/m^3 are accepted, the FAR drops from 0.51 to 0.14. Finally, and just for reference, in general many more MSG-CPP clouds are identified as ice by the MSG-CPP ice phase than by the High IWC mask, showcasing the effect the different MSG-CPP parameters used in the High IWC mask have.

Compared to the High IWC mask v1 the number of DARDAR profiles identified as high IWC events improves with the High IWC mask v2, with most high DARDAR profiles with IWC > 1 g/m^3 now identified as high IWC events. Figure 9 further suggests the higher in altitude the high IWC value, the more likely it becomes that profiles with high but not extremely high maximum IWC values are identified by the High IWC mask. This is an important result, as it suggests that optically or vertically thick clouds with high IWC values lower in the troposphere are more difficult to identify by the High IWC mask.

The sensitivity of MSG-CPP parameter thresholds as presented in Figures 7 and 8 shows that, although the High IWC mask certainly can be improved, there remains some room for choosing parameters. The typical uncertainty ranges we identified are:

- Cloud water path threshold between 100 and 400 g/m^2
- Cloud top temperature threshold between 240 and 270 K
- Cloud optical thickness threshold between 5 and 20

These ranges should be kept in mind when using the High IWC mask: there is no optimal choice in MSG-CPP parameter threshold values.

3.4 Comparison between the MSG-CPP High IWC mask and RDT.

An additional analysis was performed for comparing the High IWC mask and the MF RDT mask in order to evaluate whether both masks identify similar air masses or not, and whether one mask is preferred or the two masks are complementary.

Méteo France made RDT data available for three AIRBUS events, and provided one complete day of RDT data surrounding each event. Figure 10 shows an example of the comparison between RDT and the High IWC mask. From visual inspection only it appears that for the larger RDT cells there is a considerable overlap between RDT and the High IWC mask. However, the large areas of High IWC mask appear considerably larger than the corresponding RDT area. On the other hand, small RDT cells are generally not identified by the High IWC mask. Figure 11 shows the relation between the RDT size and the fraction of pixels identified by the High IWC mask. Clearly, the larger the cell, the larger the fraction of pixels identified. Note that this relation was also found for the other events.

Combining these results the following hypothesis emerges. Small RDT cells are young fast growing cells that are not completely iced yet. Only when convection reaches a sufficient mature stage the clouds become fully iced. Once cells mature and become larger, their dynamic development ceases and the corresponding anvils and/or high altitude ice clouds become larger. Ultimately, convective activity ceases and the high altitude cirrus remains, which is more likely to be identified by the High IWC mask than by RDT. This observation appears intuitively consistent with the common conceptual meteorological model of the evolution of convection.

In summary, RDT and the High IWC mask are complementary: RDT is very well capable of identifying young, small growing convective cells, whereas the High IWC mask appears better capable of identifying mature and aging convection and/or cirrus.

3.5 Solar zenith angle bias.

The MSG-CPP High IWC mask v2 has been implemented in an operational stream and made available in near real time on the KNMI MSG-CPP web portal (http://msgcpp.knmi.nl). One of the first impressions of the results of the implementation was that there exists solar zenith angle dependence of the High IWC mask v2. It appeared that for high angles the High IWC mask had a tendency to occur at solar facing edges of clouds either associated with frontal zones or convection. This tendency appeared to visually correlate with high cloud optical thicknesses and to cause a displacement of the COT compared to for example cloud top temperature. One possible hypothesis explaining this observation is that for optically thick and/or heterogeneous cloud systems and high solar zenith angles 3D radiative effects (*e.g.* illumination/shadowing of different parts of the cloud top) become very important, and due to the non-linear relation between optical thickness and reflectance, cause larger increase of COT in the more illuminated parts than decrease in the less illuminated parts. An overall positive bias of retrieved COT at high SZA has been observed before in for example MODIS observations [Grosvenor and Wood, 2014].

To demonstrate that such a bias indeed exists we tracked and analyzed the tropical cyclone Humberto in the Northern Atlantic Ocean on 12 September 2013. Humberto was a hurricane category 1 system on the Saffir-Simpson Hurricane Wind Scale formed in the Cape Verde region west of Africa on 8 September 2013. The system remained over the western Atlantic for approximately 12 days without causing much damage other than heavy rain on the Cape Verde Islands. On 11-12 September 2013 wind speeds reached hurricane strength (source: NOAA, http://www.nhc.noaa.gov/data/tcr/AL092013_Humberto.pdf)

Because hurricanes are well defined and consist of fully developed cloud systems whose morphology and physical properties generally do not change very fast during a period of 12 hours, they can be used to investigate SZA biases in the MSG-CPP output. Typically clouds of fully developed hurricanes reach up to the tropopause – resulting in fairly small changes in cloud top temperatures, and because of its energetics it is not expected that for example the amount of humidity, cloud water and precipitation will change very fast as hurricanes need a minimum sea surface temperature of 27°C to exist while the maximum SST rarely exceeds 33°C. It is therefore not expected that physical properties change dramatically during a 12 hour period for which MSG-CPP data is available.

Atmos. Meas. Tech. Discuss., doi:10.5194/amt-2016-246, 2016
Manuscript under review for journal Atmos. Meas. Tech.
Published: 25 October 2016

Figure 12 shows the time evolution of a number of MSG-CPP statistics and parameters for a 400×400 SEVIRI pixel area centered around 24.86°N, -27.33°E, which covers approximately a 20°×20° area. During this time the core of tropical hurricane Humberto was located within this area. Panel [A] shows that the number of CTT below 213 K (-60°C) was fairly constant over the 12 hour time period and slowly decreased, consistent with the reported weakening of the system on 12 September 2013. However, panel [B] shows that the occurrence of COT > 100 is strongly peaked at the beginning (09:00-11:00 UTC) and the end (18:00-19:00 UTC) of the period, when the counts double or triple compared to the fairly constant number of occurrences of COT > 100 between 11:00 and 18:00 hours UTC. The corresponding area average SZA (panel [C]) and in particular the area average light path (1/cosine(SZA) in panel [D]) shows a similar curvature. Finally, the number of High IWC masked pixels (panel [E]) is also fairly constant over the time period.

When comparing the correlation coefficients with the average light path (1/cosine(SZA)), it is clear that the average SZA and in particular the average light path length correlates very well with the occurrence of COT > 100. A typical SZA value for which this starts to become important is 60°. Note that for large SZA the light path could be an order of magnitude larger than for small SZAs. For the hurricane system studied here this does not bias the High IWC mask counts, presumably because the characteristics of clouds associated with a hurricane – cold, optically thick clouds with lots of condensed water - are such that they always qualify for the High IWC mask. Nevertheless, it is obvious that for other types of cloud systems the High IWC mask is likely less reliable for high SZA and/or high viewing angles, and this is consistent with the visual inspection of the data. Even for the well-organized cloud system of hurricane Humberto we could visually identify small misalignments between structures related to CTT and

COT for large SZA that we could not identify for small SZA. However, it was difficult to quantify such slight misalignments hence we reverted to the more general extremely high COT's measured in the hurricane for large SZAs. If we exclude CPP measurements for SZAs > 60°, the verification statistics of the DARDAR comparison improve slightly with the POD increasing from 0.59 to 0.62, the FAR decreasing from 0.52 to 0.49 and a the CSI increasing from 0.36 to 0.39.

4. Summary and conclusions.

For the detection of potential (high latitude) high ice water content in SEVIRI geostationary satellite measurements a mask was constructed based on the results from the CPP algorithm. The mask is based on defining thresholds for a set of CPP parameters: only if all criteria are met, *i.e.* the CPP parameter values fall within the pre-defined threshold intervals, the SEVIRI pixel is masked as a High IWC event.

Evaluation of the High IWC mask with satellite measurements of active remote sensors of cloud properties (CLOUDSAT/CALIPSO combined in the DARDAR product) shows that the mask can be fine-tuned for detection of high IWC values > 1 g/m^3 in the DARDAR profiles. A detailed sensitivity analysis of SEVIRI thresholds and subsequent statistical analysis shows that a better detection of High IWC events is accompanied by more false negatives. We decided on a combination of thresholds that maximize the Critical Success Index, but readers should be aware that depending on the requirements the parameters thresholds could be changed. Furthermore, the evaluation of results against DARDAR provided some indications that the MSG-CPP High

IWC mask is more sensitive to cloud ice or cloud water in the upper part of the cloud, which is relevant for aviation purposes. This will be a focus of future research.

Comparison with results from the RDT algorithm applied to the same geostationary SEVIRI data showed that there are similarities and differences with the High IWC mask: the RDT algorithm is very capable of detection young/new convective cells and areas, whereas the High IWC mask appears to be better capable of detecting more mature and ageing convection as well as cirrus remnants. This is likely related to the fact the RDT is developed for detecting fast growing thunderstorms which may not have that much High IWC yet. Once dynamical development of thunderstorms and convective systems ceases, RDT is unable to identify those regions but the High IWC mask still can as there is sufficient ice remaining.

Visual inspection of High IWC mask fields suggested that there could be solar zenith angle dependent biases in some of the MSG-CPP products. An analysis of a hurricane system in the tropical Atlantic (Humberto, September 2013) revealed that the MSG-CPP COT can be biased for high solar zenith angles as the light path through high altitude (ice) clouds can become very large and will not be fully representative of the real vertical cloud structure anymore. Under such circumstances, the High IWC mask can be biased, although for the Humberto we did not find evidence of increased High IWC mask occurrences, probably because hurricane systems will always be characterized by generally High IWC throughout the system. Nevertheless, some care has to be taken with the High IWC mask under conditions of extreme solar zenith angles and extreme viewing angles, and a first estimate indicates that excluding MSG-CPP measurements with SZAs > 60° slightly improves the verification statistics of the comparison of the High IWC mask with the DARDAR measurements. Note that it is equally likely that similar errors may occur due to the viewing geometry, something that we believe we could also identify visually but which was difficult to characterize quantitatively.

Although the High IWC mask is successful at detecting high IWC values in IWC profiles measured by active remote sensing sensors, it should be noted that it remains unclear what the exact conditions are of In-Service icing. It is well established that high IWC values are likely a condition for the occurrence of In Service icing, but clearly it is not the only condition for these occurrences. The lack of detailed understanding what causes such events precludes further fine-tuning of the High IWC mask.

Finally, it has been suggested that apart from icing occurring within the cores of rapidly growing and/or mature convection – with potentially a lot of super-cooled water – the majority of such events occurred in older/aged cirrus with large number densities. However, this is not a settled issue, although hopefully future field campaigns will enable a better characterization of the In-Service icing conditions. The HAIC field campaigns in 2015 and 2016 should provide more and better details of these conditions, and will be used to further evaluate the MSG-CPP High IWC mask.

Atmospheric Measurement Techniques Discussions

Acknowledgments

We thank the ICARE Data and Services Center for providing access to the DARDAR, data used in this study.

References

Autonès, F., 2012, Algorithm Theoretical Basis Document for "Rapid Development Thunderstorms" (RDT-PGE11 v2.3), SAF/NWC/CDOP/MFT/SCI/ATBD/11, available at: https://www.nwcsaf.org/scidocs/Documentation/SAF-NWC-CDOP2-MFT-SCI-ATBD-11_v3.0.pdf

Bragg, M.B., T. Basar, W.R. Perkins, M.S. Selig, P.G. Voulgaris, J.W. Melody, and N.B. Sarter, Smart icing systems for aircraft icing safety. AIAA Paper, 813, 2002.

Brown, P.R. A., and P.N. Francis, Improved measurements of the ice water content in cirrus using a total-water probe, J. Atmos. Oceanic Technol., 12, 410–414, doi:10.1175/1520-0426(1995)012<0410:IMOTIW>2.0.CO;2, 2005.

Delanoë, J., and R.J. Hogan, A variational scheme for retrieving ice cloud properties from combined radar, lidar, and infrared radiometer, J. Geophys. Res., 113, D07204, doi:10.1029/2007JD009000, 2008.

Ceccaldi M., J. Delanoë, R.J. Hogan, N.L. Pounder, A. Protat., J. Pelon, From CloudSat-CALIPSO to EarthCare: Evolution of the DARDAR cloud classification and its comparison to

Atmos. Meas. Tech. Discuss., doi:10.5194/amt-2016-246, 2016
Manuscript under review for journal Atmos. Meas. Tech.
Published: 25 October 2016

airborne radar-lidar observations. Journal of Geophysical Research - Atmospheres, 118 (14), pp. 7962-7981., doi:10.1002/jgrd.50579, 2013

Delanoë, J., and R.J. Hogan, Combined CloudSat-CALIPSO-MODIS retrievals of the properties of ice clouds, J. Geophys. Res., 115, D00H29, doi:10.1029/2009JD012346, 2010.

Delanoë, J., A. Protat, J. Testud, D. Bouniol, A.J. Heymsfield, A. Bansemer, P.R.A. Brown, and R.M. Forbes. Statistical properties of the normalized ice particle size distribution. J. Geophys. Res., 110, D10201, doi:10.1029/2004JD005405, 2005.

Delanoë, J., R.J. Hogan, R.M. Forbes, A. Bodas-Salcedo, and T.H.M. Stein, Evaluation of ice cloud representation in the ECMWF and UK Met Office models using CloudSat and CALIPSO data, Q. J. R. Meteorol. Soc., Part B, 137, 2064–2078, doi:10.1002/qj.882, 2011.

Delanoë J., A.J. Heymsfield, A. Protat A., A. Bansemer, and R.J. Hogan, Normalized particle size distribution for remote sensing application. Journal of Geophysical Research : Atmospheres, American Geophysical Union (AGU),119 (7), pp. 4204-4227., doi:10.1002/2013JD020700, 2014.

Feofilov, A.G., C.J. Stubenrauch, and J. Delanoë, J., Ice water content vertical profiles of high-level clouds: classification and impact on radiative fluxes, Atmos. Chem. Phys., 15, 12327-12344, doi:10.5194/acp-15-12327-2015, 2015.

Francis, P.N., P. Hignett, and A. Macke, The retrieval of cirrus cloud properties from aircraft multi-spectral reflectance measurements during EUCREX'93, Q. J. R. Meteorol. Soc., 124, 1273–1291, doi:10.1002/qj.49712454812, 1998.

Greuell, W., E. van Meijgaard, N. Clerbaux, and J.F. Meirink, Evaluation of model-predicted top-of- atmosphere radiation and cloud parameters over Africa with observations from GERB and SEVIRI, J. Climate, 24, 4015–4036, 2011.

Grosvenor, D.P. and R. Wood, The effect of solar zenith angle on MODIS cloud optical and microphysical retrievals within marine liquid water clouds, Atmos. Chem. Phys., 14, 7291-7321, doi:10.5194/acp-14-7291-2014, 2014.

Grzych, M.L., and J.G. Mason, Weather Conditions Associated with Jet Engine Power-loss and Damage Due to Ingestion of Ice Particles: What We've Learned Through 2009, In: 14th Conference on Aviation, Range and Aerospace Meteorology, 2010.

Hamann, U., A, Walther, B. Baum, R. Bennartz, L. Bugliaro, M. Derrien, P.N. Francis, A. Heidinger, S. Joro, A. Kniffka, H. Le Gléau, M. Lockhoff, H.-J. Lutz, J.F. Meirink, P. Minnis, R. Palikonda, R. Roebeling, A. Thoss, S. Platnick, P. Watts, and G. Wind, Remote sensing of cloud top pressure/height from SEVIRI: analysis of ten current retrieval algorithms, Atmos. Meas. Tech., 7, 2839-2867, doi:10.5194/amt-7-2839-2014, 2014.

Hess, M., R.B.A. Koelemeijer, and P. Stammes, Scattering matrices of imperfect hexagonal ice crystals, J. Quant. Spectrosc. Ra., 60(3), 301–308, 1998.

Hogan, R.J., Fast approximate calculation of multiply scattered lidar returns, Appl. Opt., 45, 5984–5992, doi:10.1364/AO.45.005984, 2006.

Mason, J.G., J.W. Strapp, and P.Chow, The ice particle threat to engines in flight. In 44th AIAA Aerospace Sciences Meeting (Vol. 4, pp. 2445-2465), 2006.

McFarquhar, G.M., and A.J. Heymsfield, The definition and significance of an effective radius for ice clouds. Journal of the atmospheric sciences, 55(11), 2039-2052, 1998.

Mecikalski, J.R., W.F. Feltz, J.J Murray, D.B. Johnson, K.M. Bedka, S.T. Bedka, and E. Williams, Aviation Applications for Satellite-Based Observations of Cloud Properties, Convection Initiation, In-Flight Icing, Turbulence, and Volcanic Ash., Bulletin of the American Meteorological Society, 88, 1589, 2007.

Meirink, J.F., Algorithm Theoretical Basis Document for Cloud Physical Products from SEVIRI, Tech. Rep. SAF/CM/KNMI/ATBD/SEV/CPP, Issue 1, Rev. 2, CM-SAF, 2013.

Mitchell, D.L., R.P. Lawson, and B. Baker, Understanding effective diameter and its application to terrestrial radiation in ice clouds, Atmos. Chem. Phys., 11, 3417-3429, doi:10.5194/acp-11-3417-2011, 2011.

Moody, E.G., M.D. King., S. Platnick, C.B. Schaaf, and F. Gao, Spatially complete global spectral surface albedos: value-added datasets derived from Terra MODIS land products, IEEE T. Geosci. Remote S., 43, 144–158, 2005.

Nakajima, T. and M.D. King, Determination of the optical thickness and effective particle radius of clouds from reflected solar radiation measurements, part 1: Theory, J. Atmos. Sci., 47, 1878–1893, 1990.

Perkins, W.R., N.B. Sarter, T. Basar, P.G. Voulgaris, H.M. Gurbacki, J.W. Melody, and S.A. McCray, An interdisciplinary approach to inflight aircraft icing safety (pp. 98-0095), AIAA, 1998.

Platnick, S., Vertical photon transport in cloud remote sensing problems, J. Geophys. Res., 105(D18), 22919–22935, doi:10.1029/2000JD900333, 2000.

Roebeling, R.A. and E. van Meijgaard, Evaluation of the daylight cycle of model-predicted cloud amount and condensed water path over Europe with observations from MSG SEVIRI, J. Climate, 22, 1749–1766, 2009.

Roebeling, R.A., A.J. Feijt, and P. Stammes, Cloud property retrievals for climate monitoring: implications of differences between SEVIRI on METEOSAT-8 and AVHRR on NOAA-17, J. Geophys. Res., 111, D20 210, 2006.

Roebeling, R.A., H.M. Deneke, and A.J. Feijt, Validation of cloud liquid water path retrievals from SEVIRI using one year of CloudNET observations, J. Appl. Meteorol. Clim., 47, 206–222, 2008.

Rossow, W.B. and R.A. Schiffer, Advances in understanding clouds from ISCCP, B. Am. Meteorol. Soc., 80, 2261–2287, 1999.

Stammes, P., Spectral radiance modelling in the UV-Visible range, in: IRS 2000: Current problems in Atmospheric Radiation, edited by W.L. Smith and Y.M. Timofeyev, pp. 385–388, A. Deepak, Hampton, VA, 2001.

Stein, T.H.M., J. Delanoë, and R.J. Hogan, A comparison among four different retrieval methods for ice-cloud properties using data from CloudSat, CALIPSO, and MODIS, J. Appl. Meteorol. Climatol., 50, 1952–1969, doi:10.1175/2011JAMC2646.1, 2011.

Stephens, G.: Radiation profiles in extended water clouds, II: Parameterization schemes, J. Atmos. Sci., 35, 2123–2132, 1978.

Wolters, E.L.A., R.A. Roebeling, and A.J. Feijt, Evaluation of cloud-phase retrieval methods for SEVIRI on Meteosat-8 using ground-based lidar and cloud radar data, J. Appl. Meteorol. Clim., 47, 1723–1738, 2008.

Wu, A., X. Xiong, D.R. Doelling, D. Morstad, A. Angal, and R. Bhatt, Characterization of Terra and Aqua MODIS VIS, NIR, and SWIR spectral bands' calibration stability, IEEE T. Geosci. Remote S., 51, 4330–4338, 2013.

Atmos. Meas. Tech. Discuss., doi:10.5194/amt-2016-246, 2016
Manuscript under review for journal Atmos. Meas. Tech.
Published: 25 October 2016

Atmospheric Measurement Techniques
Open Access
EGU
Discussions

CPP variable	Threshold value
Cloud Phase	ice
Effective Radius	> 10 µm
Condensed Water Path	> 1000 g/m^2
Cloud Top Height	> 8 km
Cloud Top Temperature	< 225 K

Table 1: CPP threshold values for the High IWC mask v1.

DARDAR / MSG-CPP	IWC_{MAX} > 1 g/m^3	IWC_{MAX} < 1 g/m^3
High IWC mask = True	**[A]** True (true positive)	**[B]** False (false positive)
High IWC mask = False	**[C]** False (false negative)	**[D]** True (true negative)

Table 2. Decision table for MSG-CPP High IWC mask

CWP [g/m^2]	[%]	CTT [K]	[%]	COT [-]	[%]	H [km]	[%]
100	8	235	2	0	21	0	2
200	10	240	6	10	22	1	7
300	19	245	9	20	32	2	12
400	18	250	10	30	19	3	16
500	21	255	13	40	3	4	21
600	11	260	14	50	0	5	26
700	8	265	14	60	0	6	13
800	0	270	14	70	0	7	0
900	0	275	14	80	0	8	0

Table 3. Fraction of High IWC masks with MSG-CPP parameter threshold values larger than the value given in the table and for which the CSI was larger than 0.35. As an example: H indicates the height of the maximum IWC value in the DARDAR profile.

Atmos. Meas. Tech. Discuss., doi:10.5194/amt-2016-246, 2016
Manuscript under review for journal Atmos. Meas. Tech.
Published: 25 October 2016

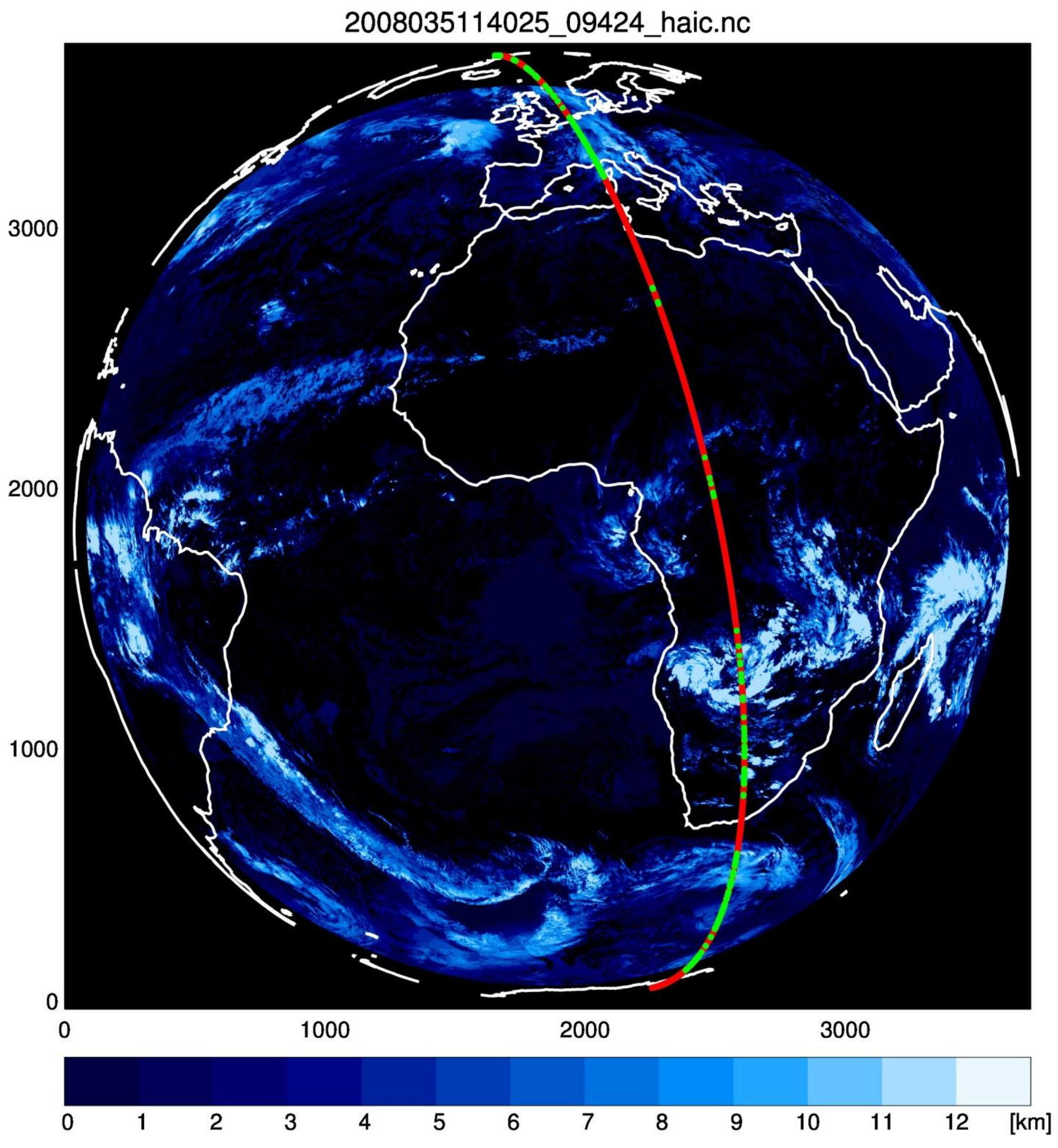

Figure 1. DARDAR orbit (4 February 2008, 12:29:56 UTC equator crossing time) and corresponding MSG-CPP cloud top height (4 February 2008, 12:30 UTC). The DARDAR orbit is shown by the red or green dots, with the green dots indicating DARDAR profiles with ice in it

and the red dots indicating DARDAR profiles without ice in it. Note that the time of MSG-CPP image is nearest to the DARDAR equator crossing time.

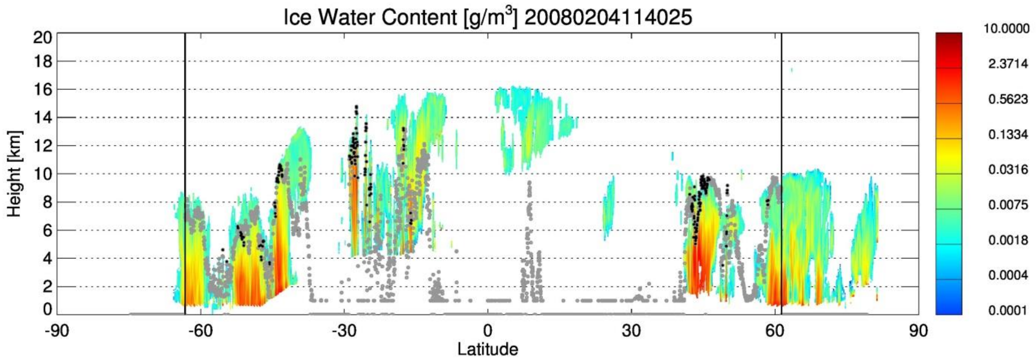

Figure 2. Cross section of DARDAR ice water content and corresponding MSG-CPP cloud top height (grey/black dots) as shown in Figure 1. The black dots denote the MSG-CPP pixels for which the High IWC mask was identified. The vertical bars indicate the geographical range for which MSG-CPP measurements are available due to the need of MSG-CPP for daytime observations.

Atmos. Meas. Tech. Discuss., doi:10.5194/amt-2016-246, 2016
Manuscript under review for journal Atmos. Meas. Tech.
Published: 25 October 2016

Atmospheric Measurement Techniques
Discussions

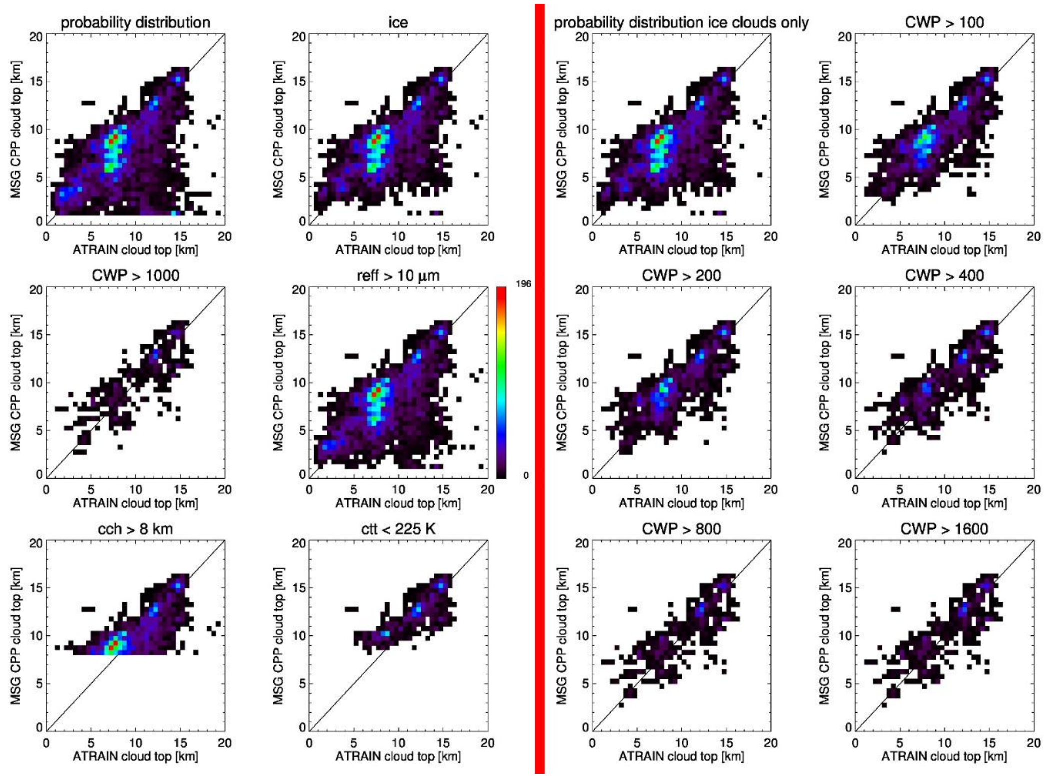

Figure 3. Probability distribution of cloud top heights estimated from MSG-CPP and A-Train/DARDAR data (highest level with IWC > 0) as function of MSG-CPP parameter values for approximately 160,000 DARDAR profile measurements obtained from 31 DARDAR orbits. The left section shows the effect of the different High IWC mask thresholds, the right section shows the effect of different CWP thresholds.

Atmos. Meas. Tech. Discuss., doi:10.5194/amt-2016-246, 2016
Manuscript under review for journal Atmos. Meas. Tech.
Published: 25 October 2016

Atmospheric Measurement Techniques
Open Access
Discussions

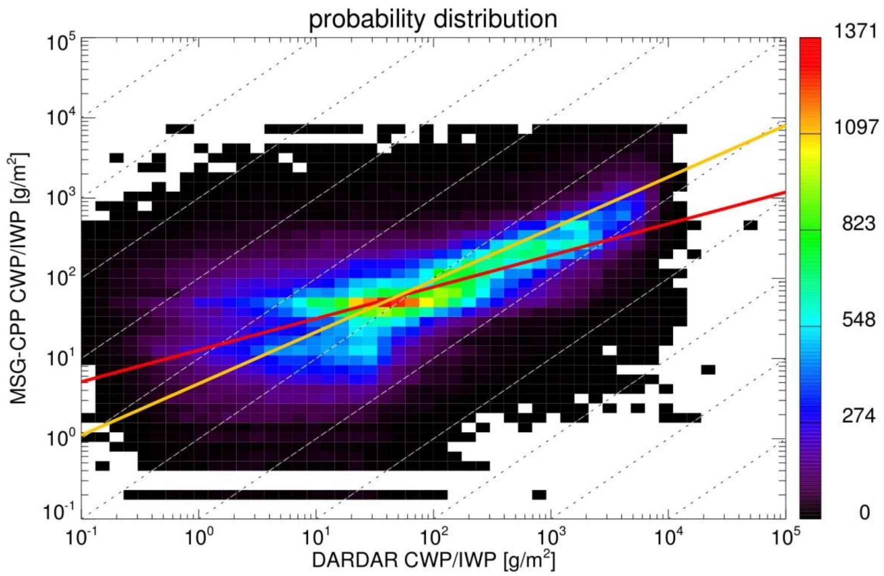

Figure 4. Probability distribution of CWP or IWP from MSG-CPP vs DARDAR for the orbits in table 2 combined. Two different linear fits are indicated with (orange) and without (red) forcing intercept of zero, but are for visualization purposes only.

Atmos. Meas. Tech. Discuss., doi:10.5194/amt-2016-246, 2016
Manuscript under review for journal Atmos. Meas. Tech.
Published: 25 October 2016

Atmospheric Measurement Techniques
Discussions

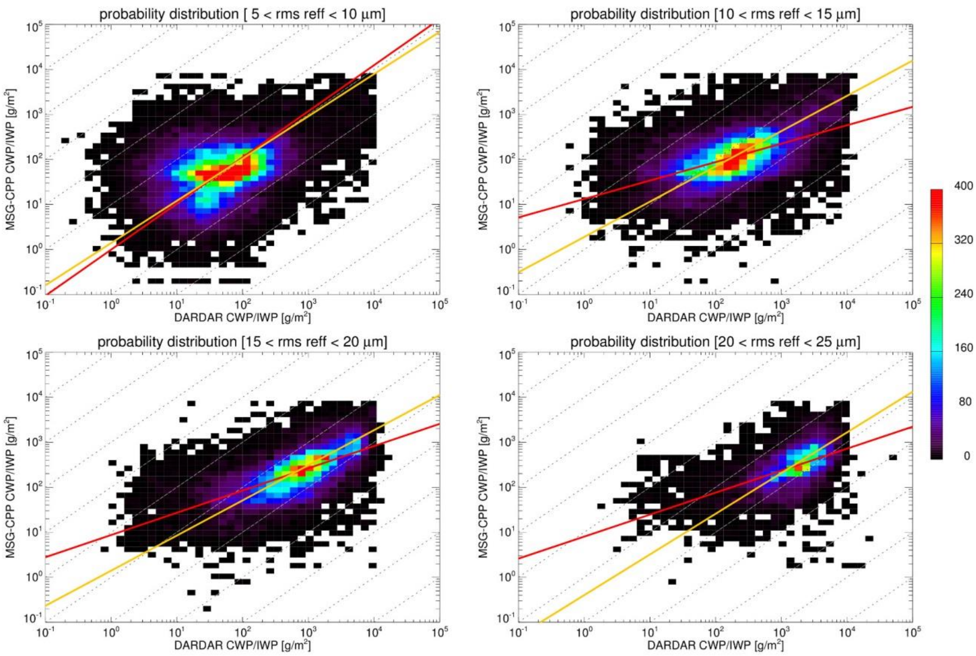

Figure 5. As Figure 4 but filtered according to the root-mean-square value of the effective radius of each DARDAR effective radius profile.

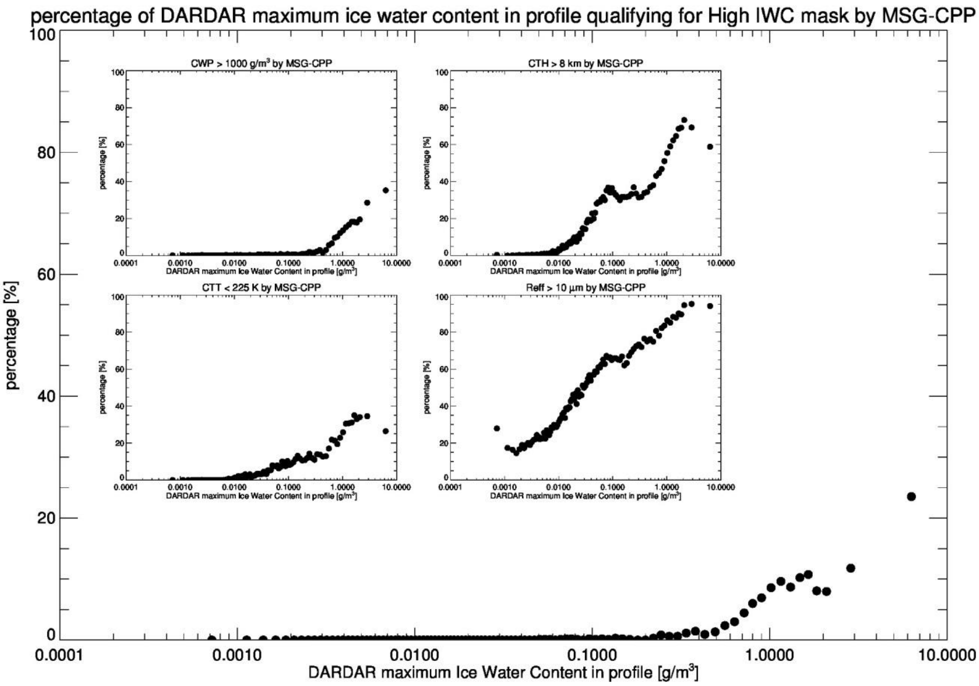

Figure 6. Fraction of DARDAR profiles (table 2) identified by MSG-CPP High IWC. DARDAR profiles are sampled according to the maximum IWC value within the profile. The insert shows the same statistic but for different MSG-CPP parameter thresholds used in the MSG-CPP High IWC mask v1 separately.

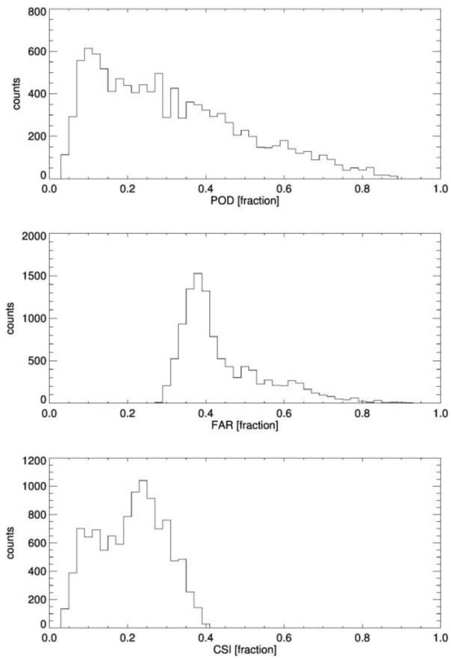

Figure 7. The MSG-CPP parameter threshold settings were varied as follows: 100 < CWP < 1000 with steps of 100 g/m^2, 225 < CTT < 275 with steps of 5 K, 0 < COT < 100 with steps of 10 [-], and the height of the maximum IWC values in the DARDAR profile varying between 1-9 with steps of 1 km.

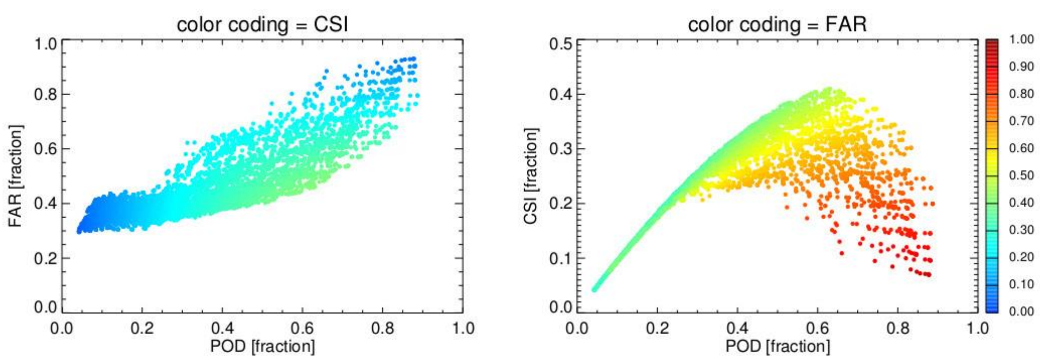

Atmospheric Measurement Techniques Discussions

Figure 8. False Acceptance Rate (FAR) and Critical Success Index (CSI) as function of the Probability Of Detection for different definitions of the MSG-CPP High IWC mask definitions and their success in detecting High IWC values in DARDAR IWC profile data. The definitions of POD, FAR and CSI and the range of CPP parameter thresholds which were varied for the High IWC mask versions can be found in the corresponding paragraph of the paper.

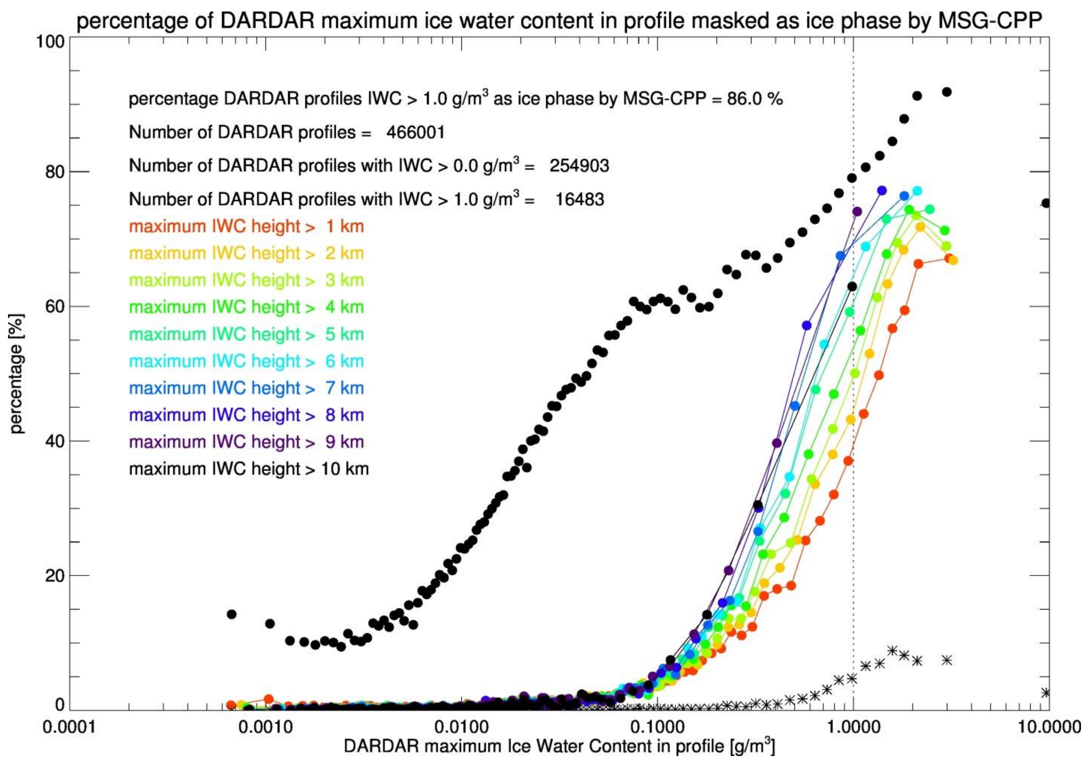

Figure 9. Similar to Figure 6 (asterisks, High IWC mask v1) but for High IWC mask v2. The black dots indicate the number of MSG-CPP cloud identified as ice given the maximum IWC within the DARDAR profile. The colored lines indicate the percentage of MSG-CPP pixels that qualify for the High IWC mask v2 pixels for DARDAR profiles with

Atmos. Meas. Tech. Discuss., doi:10.5194/amt-2016-246, 2016
Manuscript under review for journal Atmos. Meas. Tech.
Published: 25 October 2016

the height of the maximum IWC above the given altitude. See the main document for a description of the corresponding MSG-CPP parameter thresholds.

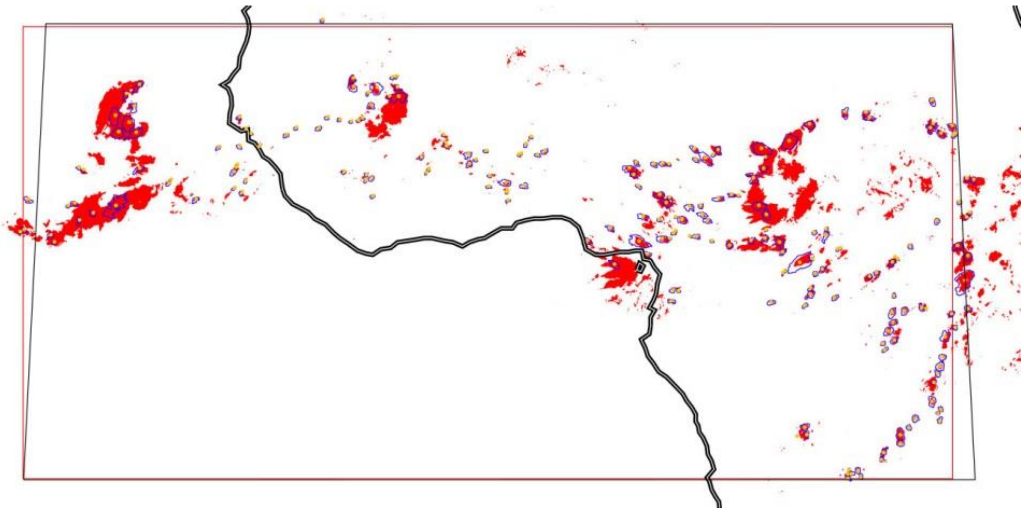

Figure 10. An example of the comparison between RDT areas (blue outlines) and the High IWC mask (red). RDT and the High IWC mask are taken at (7 September 2009 13:15:00 UTC. The orange dots indicate the center of the RDT areas. The black and red boxes are for visualization purposes only.

Atmos. Meas. Tech. Discuss., doi:10.5194/amt-2016-246, 2016
Manuscript under review for journal Atmos. Meas. Tech.
Published: 25 October 2016

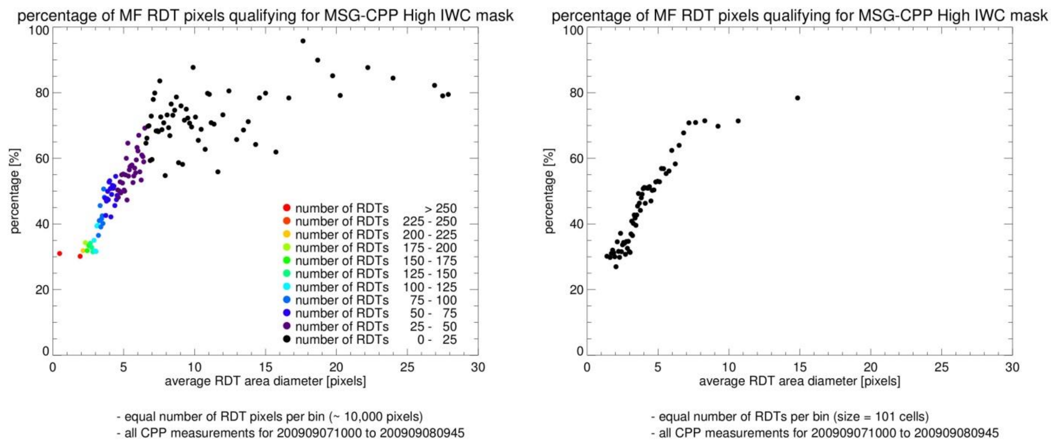

Figure 11. Correlation between average RDT area (square root of number of pixels with RDT cell) and fraction of pixels per cell identified by the High IWC mask for AIRBUS event 24. For the left plot each dot represents approximately of 10,000 RTD pixels, for the right plot each dot represents an equal number of RDT cells. The color coding in the left plot indicates the number of RTD cells for each dot. The Figures represent one 24-hour period of RDT and MSG-CPP measurements on 7 and 8 September 2009.

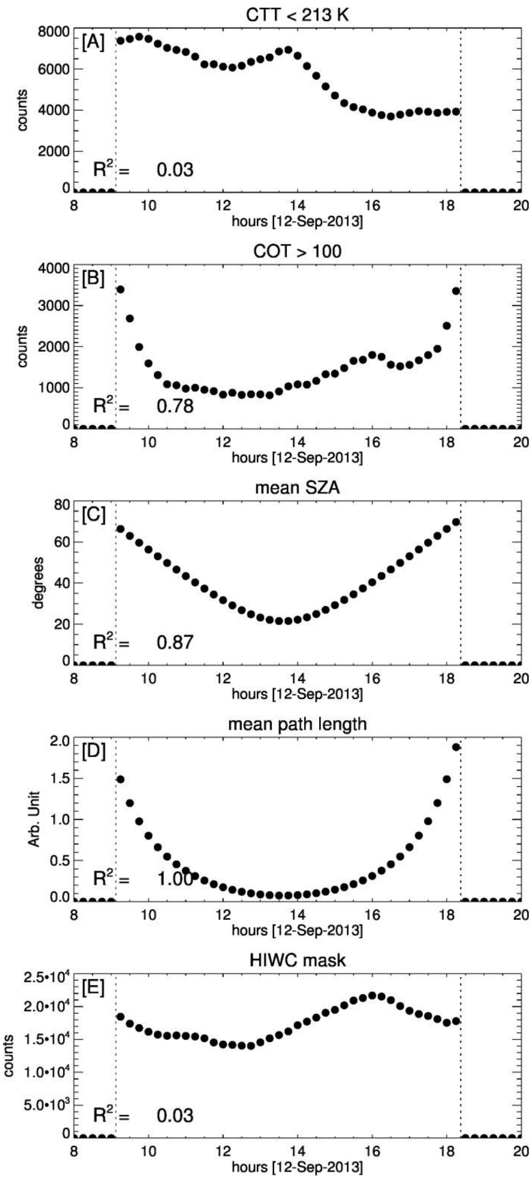

Figure 12. SEVIRI and MSG-CPP statistics of tropical hurricane Humberto on 12 September 2013. Panel [A] shows the number of SEVIRI pixels with cloud top temperatures < 213K (-60°C), panel [B] shows the number of SEVIRI pixels with CTO > 100, panel [C] shows the average SZA for the area, panel [D] shows the mean path length (1/cos(SZA)) of the area and

panel [E] shows the number of SEVIRI pixels qualifying for the MSG-CPP High IWC mask. Between the dotted lines are the times when for all SEVIRI pixels within the area MSG-CPP data was available. The correlation coefficients denote the time correlation of the parameter shown within the panel and the mean path length in panel [D], and only for the period between the dotted lines.